

See discussions, stats, and author profiles for this publication at: <https://www.researchgate.net/publication/231377465>

Comprehensive CFD Simulation of Product Yields and Coking Rates for a Floor- and Wall-Fired Naphtha Cracking Furnace

ARTICLE *in* INDUSTRIAL & ENGINEERING CHEMISTRY RESEARCH · NOVEMBER 2011

Impact Factor: 2.59 · DOI: 10.1021/ie2012642

CITATIONS

9

READS

29

5 AUTHORS, INCLUDING:



Guihua Hu

East China University of Science and Techno...

14 PUBLICATIONS 68 CITATIONS

SEE PROFILE



Yu Zhang

Ghent University

4 PUBLICATIONS 13 CITATIONS

SEE PROFILE

Comprehensive CFD Simulation of Product Yields and Coking Rates for a Floor- and Wall-Fired Naphtha Cracking Furnace

Guihua Hu, Honggang Wang, Feng Qian,* Yu Zhang, and Jinlong Li

Key Laboratory of Advanced Control and Optimization for Chemical Processes of Ministry of Education, East China University of Science and Technology, 130 Meilong Road, Shanghai 200237, People's Republic of China

Kevin M. Van Geem and Guy B. Marin

Laboratory for Chemical Technology, Ghent University, Krijgslaan 281 (S5), 9000 Gent, Belgium

S Supporting Information

ABSTRACT: A coupled furnace/reactor simulation was conducted to determine product yields and coking rates for an industrial SL-II naphtha cracking furnace fired by both floor and wall burners. The process gas side, as well as the fire side, is simulated using the computational fluid dynamics (CFD) approach. The molecular kinetic model of Kumar and co-workers was used to simulate the naphtha cracking reactions in the reactor. The results show that the asymmetrical design of the furnace results in asymmetrical profiles of flue gas velocity, temperature, and concentration, and leads to poor heat supply of the wall burners on the front wall as well as a high-temperature zone in the crossover section. The recirculation of flue gas caused by the positioning of burners makes the temperature more uniform in the middle of the furnace. Good agreement between simulation and industrial product yields has been obtained without any tuning of the kinetics, indicating that the proposed approach can be used as a guide for further optimization of geometries and operating parameters of naphtha cracking furnaces with burners located both in the floor and in the wall. The coking rate profile reveals that the maximum coking rate is not located at the coil outlet or near the last reactor bend, but rather at a height of 7 m in the second reactor pass.

1. INTRODUCTION

In a naphtha cracking furnace, many complicated physical and chemical processes such as flow, heat transfer, mass transfer, and reaction strongly interact. Combustion of fuel gas generates a large quantity of flue gas that flows in the furnace and transfers the heat to the process gas inside the reactor coil, giving rise to the complicated thermal cracking reactions. Obviously, the processes occurring in the furnace are strongly affected by the endothermic cracking reactions in the reactor coil and vice versa. The heat flux profile along the reactor coil forms the connection between process gas and flue gas side, but experimental investigation of this profile is extremely difficult, because of long cycle times, high costs, and limited measuring capabilities. Moreover, the simplified mathematical models presented by Froment,¹ Paul and Froment,² Huang et al.,³ Xie et al.,⁴ and Xu et al.⁵ are unable to take into account the improved understanding of the occurring processes in the cracking furnace. Only numerical simulation is an effective tool for optimization and design of furnaces and burners; however, these simulations are quite time-consuming and difficult to validate, because experimental data are scarce.

The research of transfer process outside and inside the reactor coil of a cracking furnace has evolved tremendously during the last two decades; from zero-dimensional model, to multidimensional model, and, more recently, to computational fluid dynamics (CFD). CFD simulation has become the standard since the early work by Detemmerman and Froment⁶ and Heynderickx et al.⁷ These authors were the first to combine a zone model and

CFD method to perform coupled simulations for the radiative heat transfer in the furnace, taking into account the thermal cracking reactions in the reactor coils. Oprins et al.⁸ and Oprins and Heynderickx⁹ continued this work and simulated the non-symmetric flow in the furnace. Stefanidis et al.^{10–13} used CFD to perform a detailed simulation for the combustion and radiation mechanism in a furnace. Fluent was also employed to conduct a coupled simulation on the combustion, heat transfer, and thermal cracking reactions in naphtha cracking furnace by Han et al.,¹⁴ Lan et al.,¹⁵ and Zhang et al.¹⁶ Wang and Zhang¹⁷ used the P-1 model to calculate radiative heat transfer, whereas Zhou and Jia¹⁸ introduced an empirical formula in the DO model for the calculation of medium radiation characteristics. However, the nozzle arrangement in the cracking furnace in the above studies was relatively simple, and combined firing using both floor burners and wall burners (i.e., the current standard for industrial naphtha cracking furnaces) has not been studied. In the work of Han et al.,¹⁴ Lan et al.,¹⁵ and Zhang et al.,¹⁶ a nonpremixed PDF model was adopted to simulate the fuel combustion process, which may lead to unexpected results for the premixed combustion process of radiation burners. The work of Wang and Zhang¹⁷ showed that the calculated precision of the P-1 model was poor for large-scale industrial

Received: June 14, 2011

Accepted: November 7, 2011

Revised: October 11, 2011

Published: November 07, 2011

furnaces with complex geometries. Zhou and Jia¹⁸ found that large errors for the absorption coefficient of gas mixture might be introduced because of the empirical formula for the radiation if the P-1 model is used. More recently, Hu et al.¹⁹ used the CFD methodology to obtain detailed information about the velocity profile, the temperature profile, and the composition of the flue gas in a naphtha cracking furnace. However, this work did not include any information about the process gas side.

In the present work, a coupled simulation for the furnace and reactor is performed in an industrial SL-II naphtha cracking furnace with 100 kt/yr capacity, in which both the floor burners and wall burners were considered. A nonpremixed combustion mechanism is adopted to account for the floor firing and a premixed combustion mechanism for the sidewall firing, respectively. A molecular model that contains 22 molecular reactions proposed by Kumar²⁰ is employed for the cracking reactions inside the reactor coil. In the present work, the profiles of temperature, velocity, and concentration of the process gas in the cracking furnace, and those of temperature, velocity, and pressure distributions of the flue gas, tube skin temperature, and heat flux profiles along the reactor tube are explicitly discussed. Particular attention is also paid to the validation, based on industrial data, and to coke formation in the cracking coil, which previously has not been done.

2. MATHEMATICAL MODELS AND PHYSICAL PROPERTIES

2.1. Furnace Model. **2.1.1. Flow Model.** The standard $k-\varepsilon$ two equations model is adopted to establish the governing equations in the furnace based on the Reynolds-averaged Navier–Stokes (RANS) equations. The continuity, momentum and energy, turbulent kinetic energy, dissipation rate of turbulent kinetic energy, and species transport equations are expressed as²¹

$$\frac{\partial(\rho\phi)}{\partial t} + \frac{\partial(\rho U_j\phi)}{\partial x_j} = \frac{\partial}{\partial x_j} \left(\Gamma_\phi \frac{\partial\phi}{\partial x_j} \right) + S_\phi \quad (1)$$

In order to bridge the viscosity-affected region between the wall and the fully turbulent region, we apply the standard wall functions based on the proposal of Launder and Spalding²² to the wall boundary conditions of the furnace and reactor.

2.1.2. Combustion Model. Most of the currently built naphtha cracking furnaces are fired with both floor burners (or also called long-flame burners) and wall burners (so-called radiation burners). In this work, the turbulence-chemistry interaction model based on the work of Magnussen and Hjertager,²³ the so-called “Finite Rate/Eddy-Dissipation model” is employed to describe the combustion occurring in both floor and wall burners. In the finite-rate model, the chemical source term is calculated using an Arrhenius expressions, in which the Arrhenius molar rate of creation/destruction of species i in reaction r is given by

$$\hat{R}_{i,r} = \Gamma(\nu''_{i,r} - \nu'_{i,r}) \left(k_{f,r} \prod_{j=1}^N [C_{j,r}]^{(\nu'_{j,r} + \eta''_{j,r})} \right) \quad (2)$$

In the Eddy-Dissipation model, the net rate of production of species i due to reaction k ($R_{i,k}$) is given by the smaller (i.e.,

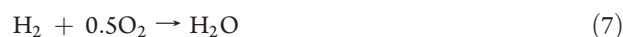
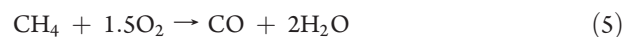
limiting value) of the two following expressions:

$$R_{i,k} = \nu'_{i,k} M_{w,i} A \rho \left(\frac{\varepsilon}{k} \right) \min \left(\frac{Y_R}{\nu'_{R,k} M_{w,R}} \right) \quad (3)$$

and

$$R_{i,k} = \nu'_{i,k} M_{w,i} A B \rho \left(\frac{\varepsilon}{k} \right) \frac{\sum_p Y_p^p}{\sum_j \nu''_{j,k} M_{w,j}} \quad (4)$$

In this model, we take the minimum of the Arrhenius (eq 2) and the Eddy-Dissipation (eqs 3 and 4) reaction rates for combustion. Methane and hydrogen combustion is represented by a simplified reaction scheme given by



2.1.3. Radiation Model. Radiation is the predominant mode of heat transfer in the cracking furnace, because of the high temperature of the combustion gases and that of the furnace wall. In this work, the discrete ordinate (DO) method is employed to solve the radiative transfer equation (RTE). The DO model is simple, reliable, and especially suitable for the coupled calculation of flow, combustion, and heat-transfer process. The generalized equation in the DO model is given by

$$\nabla \cdot (I(\vec{r}, \vec{s}) \vec{s}) + (\alpha + \sigma_s) I(\vec{r}, \vec{s}) = \alpha n^2 \left(\frac{\sigma T^4}{\pi} \right) + \frac{\sigma_s}{4\pi} \int_0^{4\pi} I(\vec{r}, \vec{s}') \Phi(\vec{s} \cdot \vec{s}') d\Omega' \quad (8)$$

In eq 8, the radiative heat transfer in the furnace can be calculated if the absorption coefficient of the flue gas is known. Several methods can be used for the calculation of the absorption coefficient of flue gas, such as the chart method, an algebraic model, the weighted-sum-of-gray-gases model (WSGGM), the wide-band model, the narrow-band model, and the line-by-line model. Among these methods, the WSGGM is the better choice, because of its higher computational accuracy and efficiency, compared with other approaches. In the present simulation, the emissivity of the real gas is expressed as the weighted sum of the emissivities of several gray gases and a transparent gas:²⁴

$$\varepsilon = \sum_{i=0}^I \alpha_{\varepsilon,i}(T) (1 - e^{-k_i p s}) \quad (9)$$

where the quantity given in the bracket is the i th fictitious gray gas emissivity.

For the DO radiation model, the wall surface temperature is calculated from the following equation,²⁵ while imposing q_{out} :

$$q_{\text{out}} = (1 - \varepsilon_w) q_{\text{in}} + n^2 \varepsilon_w \sigma T_w^4 \quad (10)$$

where

$$q_{\text{in}} = \int_{\vec{s} \cdot \vec{n} > 0}^{4\pi} I_{\text{in}} \vec{s} \cdot \vec{n} d\Omega \quad (11)$$

where I_{in} is the intensity of the incoming ray, Ω the hemispherical solid angle, and \vec{n} the normal pointing out of the domain.

The boundary intensity for all outgoing directions \vec{s} at the wall is given by

$$I_0 = \frac{q_{\text{out}}}{\pi} \quad (12)$$

Hence, the terms on the right-hand side of the energy equation of eq 1 are equal to the heat flux due to volumetric heat sources within the solid, and is given by

$$S_h = \alpha \left(\int_{4\pi} I(r, \hat{s}) d\Omega - 4\sigma T^4 \right) \quad (13)$$

2.2. Reactor Model. *2.2.1. Thermal Cracking Kinetic and Coking Model.* Naphtha is a complex mixture of hydrocarbons consisting of hundreds of different components. The detailed characterization is not straightforward and requires sometimes advanced analytical techniques.²⁶ The complexity of the feed is one of the reasons why, over the past 40 years, various kinetic models have been developed for thermal cracking of naphtha and heavier feeds.²⁷ The most advanced kinetic models, such as COILSIM²⁸ or SPYRO,²⁹ are based on the free-radical mechanism. These models are currently too complex to be used in CFD simulations, because of the overall dimensions of the resulting numerical problem and the correspondingly required CPU time.³⁰ The overall dimensions of the numerical problem is proportional to the product between the number of computational cells, which discretize the equipment, and the number of chemical species, along with a few additional variables (e.g., temperature, pressure, and momentum). Hence, for the steam cracking of naphtha, there would be some hundreds of millions of variables describing the coupled CFD and kinetic problem if a complex kinetic scheme such as that implemented in COILSIM or SPYRO would be used. Currently, this is still computationally too demanding; therefore, we have employed the molecular kinetic model of Kumar and co-workers.²⁰ This model consists of 22 reactions, i.e., one primary reaction and 21 secondary reactions, involving 18 species. The salient feature of the Kumar model is that the secondary reactions remain unchanged for different naphtha feeds, but the selectivity coefficients of the primary reaction can be adjusted based on industrial data.

The semiempirical coking model of Plehiers^{31,32} is used for simulating the coking rate. The coking rate is then calculated via the following equation:

$$R_C = A_{C_2H_4} \exp\left(-\frac{E_{a,C_2H_4}}{RT}\right) + A_{C_3H_6} \exp\left(-\frac{E_{a,C_3H_6}}{RT}\right) \quad (14)$$

The coking model of Plehiers has been used to predict the run length of several industrial-cracking units,^{32–34} showing a good agreement between industrial and simulated results. Also, for the amount of coke obtained in the pilot plant, good agreement is obtained between simulated and experimental data.³⁵

2.2.2. Transfer Reaction Process Model. The flow field, temperature field and product yields in the reactor tube are calculated from the RANS equations with the $k-\varepsilon$ model for turbulence as the closure model. The approach in the reactor tube is very similar to that used for the furnace. The source terms in the energy, species, and continuity equations are determined by the kinetics of the occurring reactions. The kinetics are described using Arrhenius expressions. Hence, the chemical

reaction rate can then be expressed as

$$\hat{R}_{i,r} = \Gamma(\nu''_{i,r} - \nu'_{i,r}) \left(k_{f,r} \prod_N^{j=1} [C_{j,r}]^{\eta'_{j,r}} - k_{b,r} \prod_N^{j=1} [C_{j,r}]^{\eta''_{j,r}} \right) \quad (15)$$

There are 25 balance equations (i.e., 18 species balances, 3 momentum balances, 1 energy balance, 1 mass balance, 1 turbulent kinetic energy balance, and 1 dissipation rate of turbulent kinetic energy balance) that must be solved to obtain the velocity, temperature field, and pressure fields and the product yield profiles.

2.3. Physical Properties. Thermal cracking of naphtha is carried out at relatively low pressures (0.35 MPa at the inlet and 0.17 MPa at the outlet) and high temperatures (873 K at the reactor inlet and 1123 K at the reactor outlet). Hence, the process gases inside the reactor tube can be considered as ideal and, thus, the density of the mixture can be calculated by the ideal gas law:

$$\rho = \frac{p}{RT \sum (Y_i/M_i)} \quad (16)$$

The viscosity of mixture is given by

$$\mu = \sum_i \frac{X_i \mu_i}{\sum_j X_j \phi_{ij}} \quad (17)$$

where μ_i is the viscosity of a pure component i and is defined as

$$\mu_i = 2.67 \times 10^{-6} \frac{\sqrt{M_i T}}{\sigma_i \Omega_{\mu i}} \quad (18)$$

with

$$\Omega_{\mu i} = \Omega_{\mu i} \left[\frac{T}{(\varepsilon/k)_i} \right] \quad (19)$$

where σ_i and $(\varepsilon/k)_i$ are the Lennard-Jones collision diameter and potential energy parameter of component i , respectively, and their values are taken from the work of Hirschfelder et al.³⁶ In eq 20, the interaction parameter ϕ_{ij} is calculated by

$$\phi_{ij} = \frac{\left[1 + \left(\mu_i/\mu_j \right)^{1/2} (M_i/M_j)^{1/4} \right]^2}{\{ 8[1 + (M_i/M_j)] \}^{1/2}} \quad (20)$$

The heat capacity of mixture is computed from a mass fraction average of the heat capacities of pure species as

$$C_p = \sum_i Y_i C_{pi} \quad (21)$$

where C_{pi} is the heat capacity of pure species i and defined by a polynomial function of temperature:

$$C_{pi} = A_i + B_i T + C_i T^2 + D_i T^3 \quad (22)$$

where A_i , B_i , C_i , and D_i are the coefficients of heat capacity of pure species i .

For the thermal conductivity of pure species, the kinetic theory is used:

$$\lambda_i = \frac{15}{4} \left(\frac{R}{M_i} \right) \mu_i \left[\frac{4}{15} \left(\frac{C_{pi} M_i}{R} \right) + \frac{1}{3} \right] \quad (23)$$

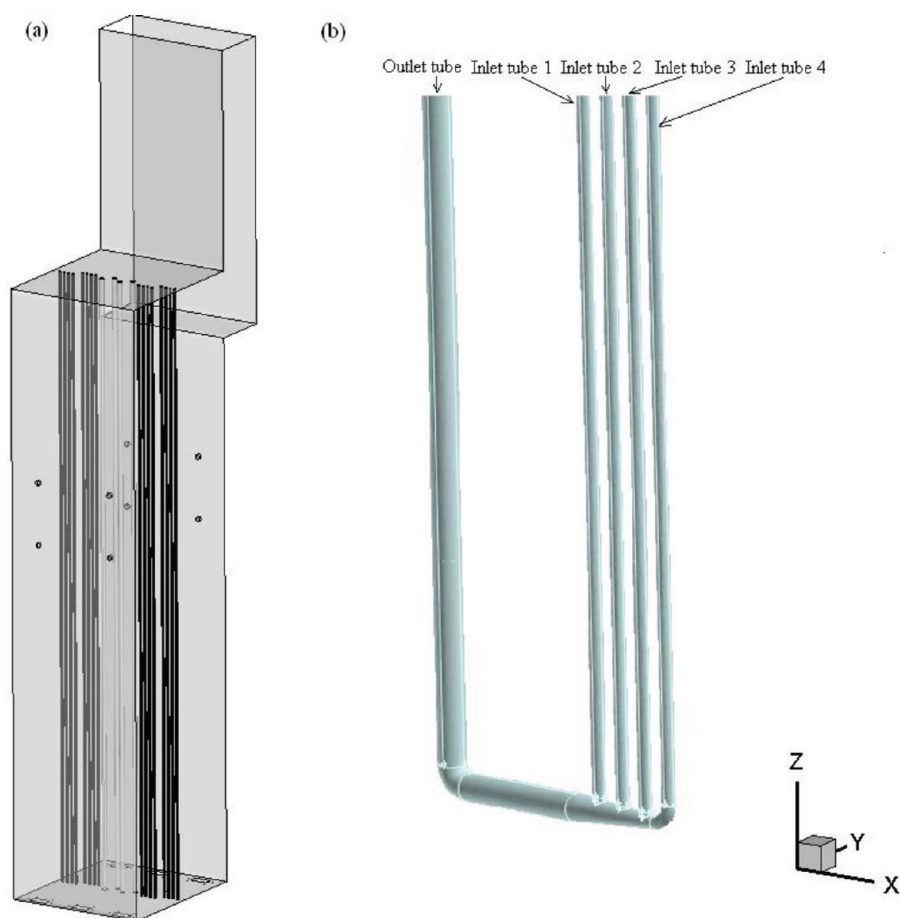


Figure 1. Schematic diagram of cracking furnace: (a) front view of the considered segment of cracking furnace and (b) SL-II coil configuration.

The thermal conductivity of mixture then can be computed by

$$\lambda = \frac{\sum_i X_i \lambda_i}{\sum_j X_j \phi_{ij}} \quad (24)$$

The binary mass diffusion coefficient for species i in species j is also computed according to the kinetic theory:

$$D_{ij} = 0.00188 \left(\frac{\{T^3 [(1/M_i) + (1/M_j)]\}^{1/2}}{p \sigma_{ij}^2 \Omega_D} \right) \quad (25)$$

where

$$\Omega_D = \Omega_D \left[\frac{T}{(\varepsilon/k)_{ij}} \right],$$

$$(\varepsilon/k)_{ij} = \sqrt{\left(\frac{\varepsilon}{k} \right)_i \left(\frac{\varepsilon}{k} \right)_j}, \quad \text{and} \quad \sigma_{ij} = \frac{1}{2}(\sigma_i + \sigma_j) \quad (26)$$

The diffusion coefficient for species i in a mixture is given as

$$D_{i,m} = \frac{1 - X_i}{\sum_{j,j \neq i} (X_j / D_{ij})} \quad (27)$$

For the calculation of physical properties of flue gas, the used methods for the density and heat capacity are similar to those of

the process gas while the viscosity and thermal conductivity are defined as a polynomial function of the temperature.

3. SIMULATION PROCEDURE

3.1. Furnace Geometry and Operating Conditions. The SL-II cracking furnace is shown in Figure 1. Only a representative segment (i.e., one-sixth) of the industrial cracking furnace is simulated because of the similarity. In the full furnace, there are 24 U-type split coils vertically suspended in the center of the furnace as a staggered arrangement in two rows. The reactor is of the “4–1” type, i.e., four inlet tubes (first pass) are linked to a single outlet tube (second pass). In the furnace floor, near the walls of both sides, 36 long-flame burners are put in two rows. Each burner includes five nozzles, where the primary nozzles are arranged in the air inlets, and other auxiliary nozzles are arranged around the air inlets. The furnace segment is heated with 48 additional radiation burners. These burners are positioned in one row in the front wall and another row in the rear wall of the furnace. The furnace outlet is located at right side of the row of reactor tubes.

Tetrahedral cells are used to discretize the physical domain including the burner zones and the tube skin zones. Hexahedral cells are used to discretize the furnace zone. The number of grid cells for the furnace is 338 860. The grid independence of our simulation results has been verified, and the results are given in the Supporting Information. A hexahedral mesh is used for the tube skin, and a mixture of grid is used for the connection part of

Table 1. Furnace Dimension and Operating Conditions

Furnace Segment	
length (<i>x</i> -direction) (m)	18.94
width (<i>y</i> -direction) (m)	3.56
height (<i>z</i> -direction) (m)	13.707
number of floor burners	36
number of wall burners	48
Firing Conditions	
fuel gas flow rate in bottom (kg/s)	1.2439
fuel gas flow rate in side (kg/s)	0.2025
oxygen excess (vol %)	2
fuel composition (wt %)	
CH ₄	97.686
H ₂	0.516
CO	0.897
C ₂ H ₄	0.899
Material Properties	
emissivity of the furnace wall	0.75
emissivity of tube skin	0.9
Reactor Coils	
number of reactor tubes	24
number of passes	2
inlet tube diameter (10 ⁻³ m)	64
outlet tube diameter (10 ⁻³ m)	121
thickness of tube (10 ⁻³ m)	6.5
feed rate (kg/s)	11.11
steam dilution (kg/kg)	0.6
coil inlet temperature (K)	883
coil outlet pressure (kPa)	206
feedstock composition (wt %)	
<i>n</i> -paraffins	46.235
<i>i</i> -paraffins	32.219
olefins	14.548
aromatics	6.997

the tube. The number of grid cells is 80 949 for a reactor coil. The geometry of the furnace and coil, as well as the operating conditions, are given in Table 1.

3.2. Boundary Conditions. The parameters of the mass flow, temperature, and mixture composition of the air and fuel gas at the inlet of the floor and wall burners used in this simulation originate from the operating conditions of the industrial furnace. This is also the case for the required parameters for the reactor simulation. The outlet boundary conditions of furnace and reactor tube are all determined as pressure outlet boundaries. The former is set to -50 Pa at the outlet of the furnace (gauge pressure), while the latter is defined as the coil outlet pressure as one listed in Table 1. The no-slip boundary condition is imposed at the reactor and furnace walls. The heat boundary on the furnace walls is calculated based on the industrial heat loss value. The skin-temperature boundary for reactor tubes is obtained from the industrial working conditions, and it is assigned to the tube skin using user-defined functions (UDFs).

3.3. Coupled Furnace/Reactor Simulation. The coupled calculation algorithm is shown in Figure 2. In the simultaneous numerical solution, several iterations are needed between these two models to reach convergence. First, an external tube

skin-temperature profile from industrial measurement is assigned as the tube-skin boundary of the furnace model using a UDF. Calculation of the combustion and heat-transfer processes inside the furnace is then carried out and the first boundary condition of heat flux profile for the reactor tubes is obtained. Next, the transfer and reaction models of the reactor tube are calculated with the resulting new reactor tube-skin temperature profile. The coupled calculation is continued until the maximal difference of tube-skin temperature between two successive iterations reaches a predefined threshold value (e.g., 1 K).

The governing equations for the conservation of mass, momentum, energy, turbulence, and radiation are solved sequentially (i.e., segregated from one another) using a control-volume-based method. The nonlinear governing equations are discretized implicitly through a second-order upwind scheme and linearized to produce a series of equations for the dependent variables in every computational cell. The Semi-Implicit Method for Pressure-Linked Equations (SIMPLE) algorithm is used to solve the coupled momentum, energy, and species transport equations.

4. RESULTS AND DISCUSSION

The reactor effluent from a naphtha steam cracker is very complex,²⁶ containing over 100 different components from hydrogen, over ethylene and propylene until naphthalene and phenanthrene. Accurately predicting the effluent composition based on the complex naphtha composition is a huge challenge. In Table 2, a comparison between simulation results and industrial data for the converged coupled furnace/reactor simulation is given. One can see that the obtained outlet temperature of the flue gas, excess oxygen ratio, coil outlet temperature (COT), residence time, coil inlet pressure (CIP), and the pressure drop over the reactor are in good agreement with the industrial data. Also, the main product yields agree well with those measured in the industrial cracker, apart from butadiene, indicating that the simulation, when performed accurately, reflects the characteristics of the flow, combustion, and thermal cracking reactions occurring in the investigated industrial furnace. The good agreement is particular surprising, because none of the kinetics has been adjusted from those reported by Kumar.²⁰ It would be possible to achieve an even better agreement if the coefficients in the primary reaction would have been modified or some of the kinetics in the secondary mechanism would have been refitted. For example, in the work of Wang et al.,³⁷ the kinetics in the Kumar model were refitted to improve the agreement between simulated and experimental data. In our case, this last approach could help to get, for example, a better agreement between the simulated and experimentally determined butadiene yield.

4.1. Tube Skin Temperature and Heat Flux Profile. In Figure 3, the tube-skin temperature profile along the reactor length is shown. Along inlet tube 1, the skin temperature increases from 994 K at the entrance to the first maximum of 1241.5 K at a tube length of ~9.5 m and then falls to 1214 K at the outlet. The tube-skin temperature of the outlet tube increases from 1202 K at the entrance to the second maximum of 1296 K at a tube length of ~20.5 m and then falls to 1185 K at the exit of the outlet tube. One can also see from Figure 3 that the tube-skin temperature at the same axial position along the inlet tube slightly decreases from inlet tubes 1, 2, and 3 to inlet tube 4, because of the different heat flux profiles along the different inlet tubes. The maximum temperature difference between them is ~4 K.

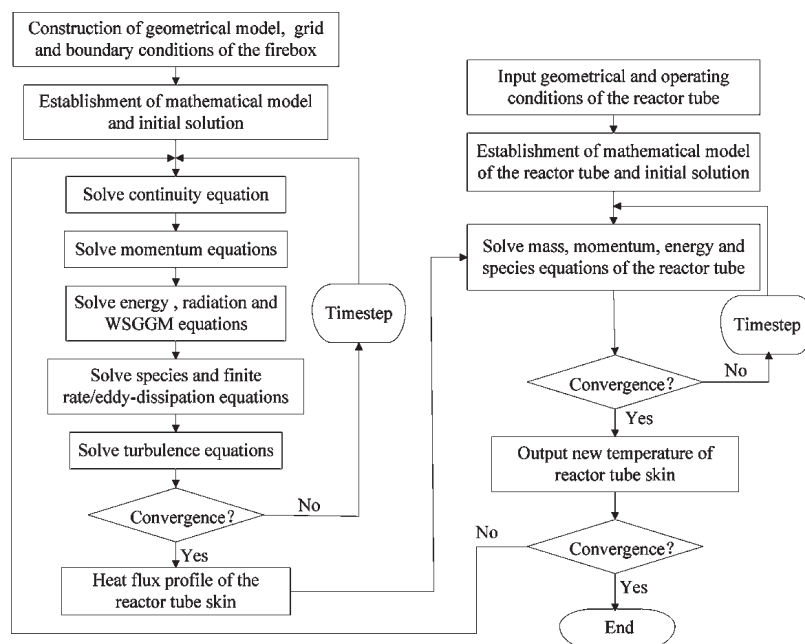


Figure 2. Flowchart of coupled solution algorithm for mathematical models in both the furnace and the reactor.

Table 2. Comparison between Simulation Results and Industrial Data

item	industrial data	simulation data
temperature of flue gas at outlet (K)	1397	1372
excess oxygen ratio (vol %)	2	1.92
temperature of process gas at outlet (K)	1108	1111
residence time (s)	0.25	0.227
coil inlet pressure (MPa)	0.2543	0.2504
coil pressure drop (MPa)	0.0433	0.0444
yield (wt %)		
C ₂ H ₄	30.64	30.21
C ₃ H ₆	15.21	15.98
CH ₄	14.86	14.20
C ₂ H ₆	3.36	3.07
C ₄ H ₈	3.66	3.40
C ₄ H ₆	4.96	2.79
C ₆ H ₆	4.25	1.56

The heat flux profiles of the tube skin along the reactor length that correspond to the skin temperature of inlet tube 1 (see Figure 3) are shown in Figure 4. The different heat flux profiles corresponding to the different convergence loops have also been added. One can see that the heat flux profiles of the different iterations are almost identical, apart from the initial section of the first pass and the last section of second pass, because of the good initial guess of the boundary conditions. The heat flux is relatively low at the beginning of the inlet tube, because of the low flue gas temperature. As the process gas temperature inside the tube increases, the endothermic cracking reactions increase, and, hence, the heat absorbed by the process gas also increases. The heat flux reaches the first peak at the tube length of ~ 7 m, where the flue gas temperature reaches its maximum. This height also

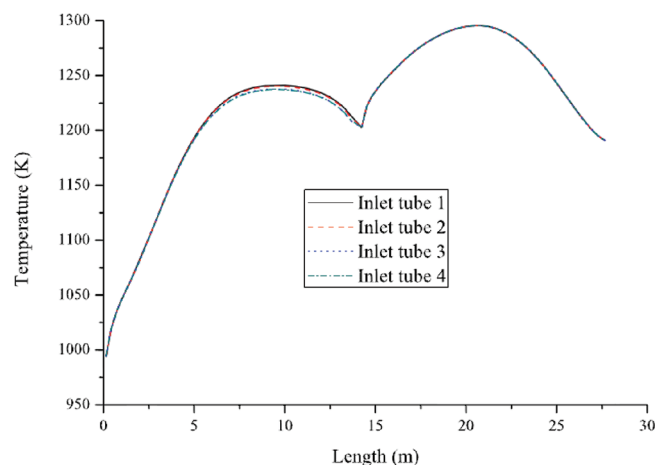


Figure 3. Tube-skin temperature profiles along the axial position of the coil.

corresponds, more or less, with the height of the flame of the floor burners. When the process gas reaches the outlet tube, it re-enters the flue gas high-temperature section, and, hence, the heat flux increases with the increase of the tube length, and reaches the second maximum at an axial position of ~ 20 m. This shape of the heat flux is in good agreement with the mathematical models for characterizing and predicting heat flux profiles by Colannino³⁸ for furnaces equipped with floor and wall burners.

4.2. Process Gas Temperature, Velocity, and Pressure Profiles. In Figures 5a–c, the profiles of temperature, velocity, and pressure of the process gas along the length of the reactor are depicted. Figure 5a shows that the process gas temperature at the same length position along the different inlet tubes slightly increases with the order of the inlet tube 1, 2, 3, and 4 (see Figure 1) and the maximum temperature difference among them is 2.4 K, which is obviously related to the difference in heat flux and tube-skin temperature profiles (see Figure 3) for these inlet

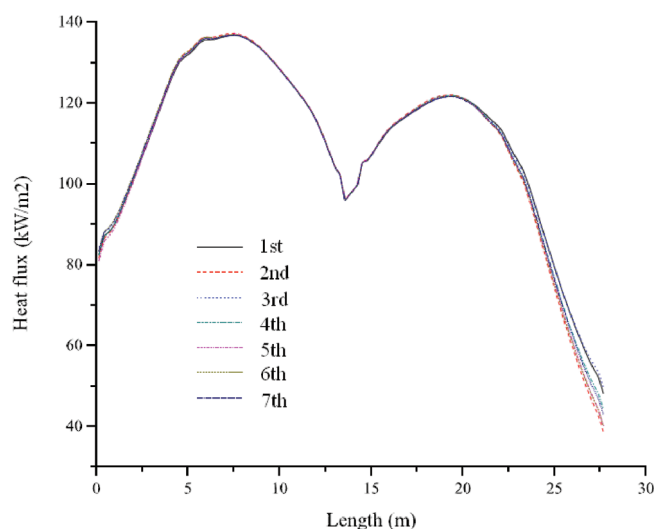


Figure 4. Heat flux profiles along the reactor length for the different iteration cycles.

tubes. In the first part of inlet tube 1, the temperature of the process gas rapidly increases because of the low process gas temperature and limited heat consumed. The temperature rapidly increases from 883 K at the entrance of inlet tube to 1039 K at the tube length of 6.5 m. With increasing process gas temperature, the reaction rate becomes larger and the absorbed heat is mainly used for the reaction; hence, the slope of the process gas temperature is reduced. At the tube bend, where the diameter changes, the temperature of the process gas has a small decline, because of a reduction of the absorbed heat due to the decrease of specific surface area, while the heat requirement for reaction inside the tubes remains high. In the following section, the reaction rate decreases and the absorbed heat is again mainly used for the temperature increase of the process gas inside the outlet tube, making the process gas temperature increase again.

Figure 5b shows that the process gas velocity gradually increases along the length of the inlet tube, because of expansion of the process gas caused by cracking of the molecules into smaller pieces. In inlet tube 1, the process gas velocity increases from 70 m/s at the entrance of inlet tube to 136 m/s at the changed-diameter site and the velocity steeply decreases from 139 m/s to 133 m/s, because of the sudden increase in the diameter of the second pass. Obviously, the increase of the process gas velocity is smaller than that in the inlet tube, because the diameter of the outlet tube is bigger, and the volume expansion of the process gas is smaller, because a significant portion of the feed was already converted. Based on the obtained average velocity, the residence time of the process gas inside the reactor tube has been calculated and it is 0.23 s, which is in good agreement with the industrial data (0.25 s). In addition, one can find from this figure that the process gas velocity at the same length position along the inlet tube length decreases from inlet tubes 1, 2, and 3 to inlet tube 4, because of the difference in expansion caused by the different heat flux profiles.

The pressure profile of process gas is illustrated in Figure 5c. As can be seen from this figure, the pressure in all of the inlet tubes decreases monotonically with the axial position. Logically, the pressure drop in the first pass is larger than that in the second pass. Furthermore, the process gas pressure along the inlet tube increases from inlet tubes 1, 2, and 3 to inlet tube 4. At the bend

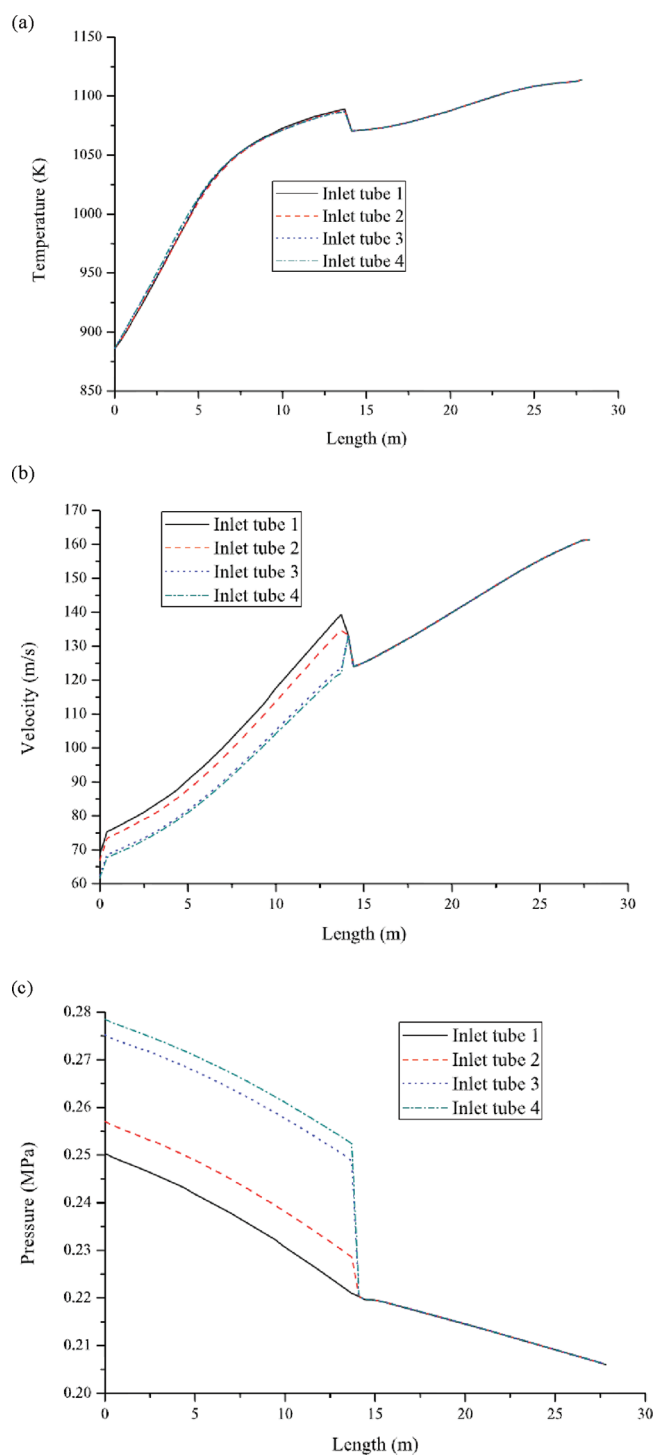


Figure 5. Process gas (a) velocity, (b) temperature, and (c) pressure profiles along the reactor length.

of the reactor tube, the slope of the pressure profile changes, consistent with the variational tube diameter design of SL-II-type coils. Based on the simulated pressure profile, the simulated pressure drop over the coil is 0.04 MPa, which agrees well with the industrial data (0.04 MPa), indicating that the calculated pressure results are reasonable.

4.3. Process Gas Concentration Profiles and Coking Rate.

The profiles of the main product yields along the axial direction

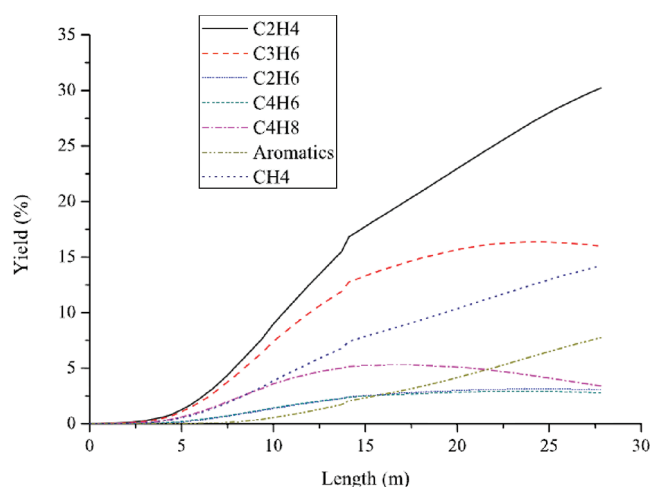


Figure 6. Profiles for the main product yields along the length of the reactor.

of the coil are depicted in Figure 6. The C_2H_4 yield initially slowly increases, because of the low temperature of the process gas. In the rear section of first pass, the process gas temperature increases further, giving rise to more and more ethylene. The C_2H_4 yield slowly increases when the process gas enters into the outlet tube, because of the decrease of reactant. The C_3H_6 yield has a different shape and reaches a maximum at ~ 25 m, because, at higher temperatures, the formed C_3H_6 will be converted to C_2H_4 and CH_4 . Also, addition reactions will ensure that some of the formed C_3H_6 is transformed to higher-molecular-weight products such as aromatics. For the yields of other components like C_2H_6 , C_4H_6 , and C_4H_8 , the trends are similar to that of C_3H_6 while the yield of CH_4 increases monotonically along the axial reactor coordinate. In general, the observed trends are in good agreement with the typical trends reported in the literature.^{20,39}

The CFD simulation of the cracking coil also allows one to address the importance of radial nonuniformities of species concentrations in the coil. Figure 7a shows the mass fraction of ethylene at a height of 3 m in the second pass reactor tube and reveals that there exist strong radial nonuniformities at this position. For other products, similar profiles are observed. This, on the one hand, is caused by nonuniformities of the temperature and velocity, as can be seen in Figures 7b and 7c. Because we are looking at a position quite close to the bend, the velocity profile has this unusual profile. On the other hand, circumferential nonuniformities in the heat flux profile also are responsible, as reported by Heyndrickx et al.⁴⁰ and shown in Figure 7d. Heynderickx et al.⁴⁰ found that, for their ethane cracking furnace, circumferential tube-skin temperatures varied by 50 °C and more, because of so-called “shadow effects.” Circular tubes suspended in cracking furnaces suffer from significant nonuniformity of tube skin temperature around tube perimeter, because of the presence of “front” and “shadow” sides on the tubes. The higher ethylene weight fraction on one side of the cross section will also cause more coke to deposit on this side than on the opposite side base. Figure 7b shows that important radial temperature gradients are simulated, on the order of 100 K, which agrees well with values reported by Van Geem et al.³⁴ and Lan et al.¹⁵ This again gives an indication that our results are reasonable.

Finally, the CFD simulation of the cracking coil also allows one to obtain an estimate for the coking rate based on the

semiempirical model of Plehiers.³¹ Naphtha steam cracking leads to an effluent containing acetylenic, olefinic, and aromatic compounds, which are known precursors for cokes formed on the inside surface of the radiant coil,^{41,42} in the convection section,⁴³ and in the transfer-line heat exchanger.⁴⁴ The coke layer inhibits heat transfer from the tube to the process gas, raises tube-wall temperatures, and reduces the cross-sectional flow area of the tube, thus increasing the pressure drop along the radiant coil.⁴⁵

Figure 8 shows the coking rate profile calculated based on the internal tube-skin temperature at four circumferential positions. For all four of these coking curves, two maxima can be observed, corresponding to the maxima in the heat flux and the external and internal wall temperature profiles. For position A in Figure 8, a small third maximum at a position of 16 m can be seen, caused by the irregularities in the flow pattern seen in Figure 7c just after the bend. The maximum coking rate is observed at ~ 21 m, which is more or less in the middle of the second pass of the reactor. Figure 8 further shows that, in the first leg, the difference in coking rate for the four circumferential positions remains small and some differences become visible only in the second pass. The circumferential differences in the temperatures and concentrations of the coke precursors are responsible for the nonuniform coking rates and, over time, will lead to nonuniform coking layers accumulating on the reactor wall. Local excessive coking can cause significant damage to the reactor material of the tubes. For the present reactor design, circumferential temperature differences of over 20 °C have been simulated. However, the difference in circumferential temperature remains limited to 4 °C there, while the coking rate reaches its maximum value. The latter implies that the simulated maximum coking rate is only slightly dependent on the circumferential position for the present reactor.

Figure 8 further shows the strong relationship between the coking rate and the wall temperature. The latter has a consequence that the coking rate does not reach a maximum at the coil outlet, where the total olefin production reaches its maximum. Also, our simulations reveal that the flow pattern has an effect on the concentration profiles along a cross section of the tube (see Figure 7a). It is obvious that measures that help to reduce the maximum wall temperature and decrease concentrations nonuniformities will have significant effects on the coking tendency of the coil. One of these measures is increasing the turbulence by using a MERT-type reactor.⁴⁶ These designs will reduce the radial temperature and concentration gradients and give better heat transfer and, hence, lower wall temperatures and, thus, coke formation.

4.4. Flue Gas Velocity Field. Figure 9 shows the flue gas velocity field at different heights in the plane at $x = 0.525$ m along the width of the furnace. The velocity distribution of the flue gas is not completely symmetrical just above both rows of floor burners. This is because the furnace outlet is located on the front wall side, while in the middle and the top of the furnace, the flue gas of the rear wall side flows to the exit of the front wall side. A large recirculation zone exists near the reactor tubes, because of the entrainment effect of the high-velocity jet of the floor burners. The height of this recirculation zone in the middle along the y -direction is ~ 9 m. The flue gas velocity decreases gradually and the velocity gradient is small because of diffusion and recirculation of flue gas between two rows of floor burners. The highlighted portion of Figure 9, labeled as “C”, is the local enlarged diagram of the other two recirculation zones in the crossover section. With the rise of flue gas along the furnace height, the flue gas encounters obstacles at the top of the furnace,

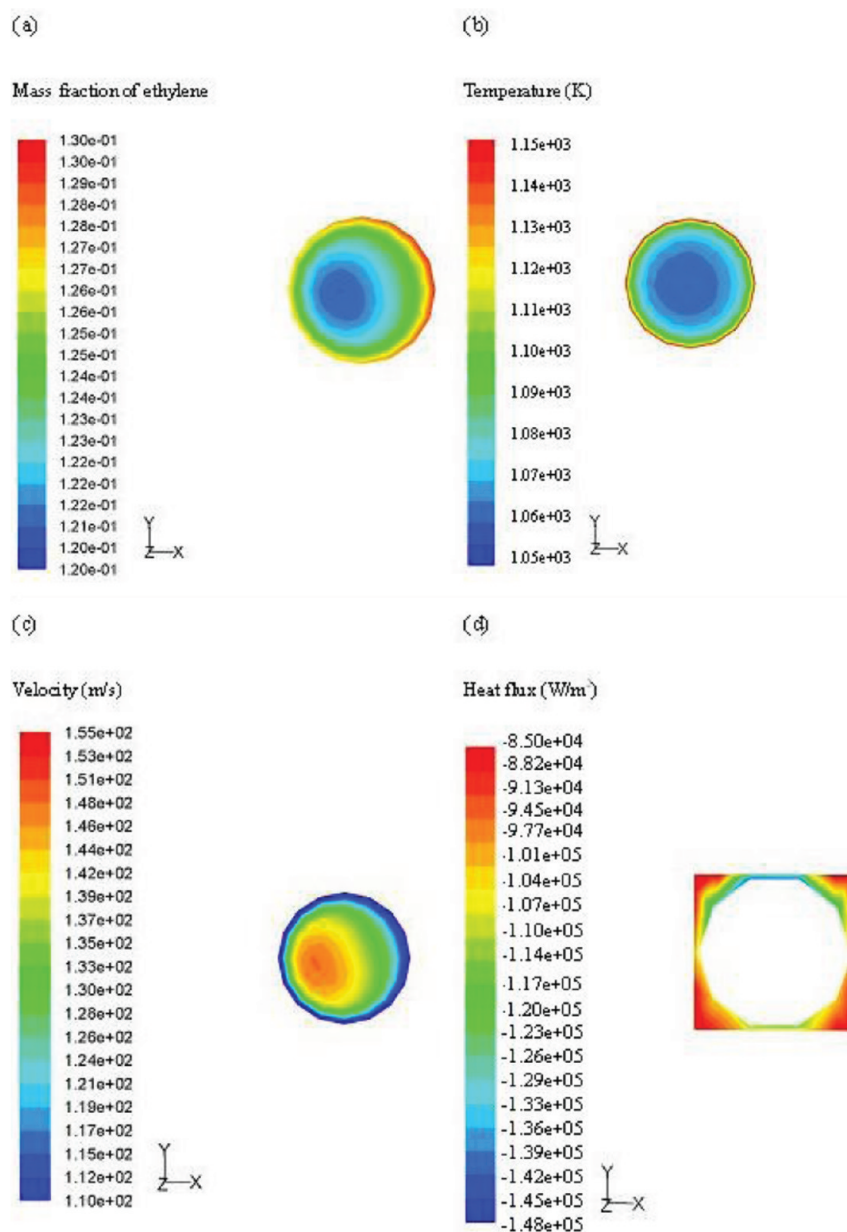


Figure 7. Radial profiles of (a) ethylene mass fraction, (b) temperature, (c) velocity, and (d) circumferential heat flux at a height of 3 m on the second pass reactor.

leading the flue gas flow direction to change and the boundary layer to be separated; hence, a recirculation zone (labeled as “A”) appears at the top corner of the furnace (see region labeled “C” in Figure 9). When the flue gas enters the convection section, it is forced to make a sharp turn where the cross section becomes small. This causes the flue gas velocity to increase, creating another recirculation zone (denoted as “B”) at the corner of the convection section inlet.

4.5. Flue Gas Temperature Profiles. Figure 10 shows the flue gas temperature contour on the cross section at $x = 0.525$ m. In Figure 10, clear temperature gradients can be observed as a function of the height and width the furnace. That is, the flue gas temperature is high near the furnace wall region, while the flue gas temperature is low near the reactor tubes region. In the bottom and top of the furnace, the temperature is very low and increases slightly near the side wall burners. The reason for this

phenomenon is the arrangement of the floor burners near the furnace wall in order to prevent the flame produced from direct impingement on the tubes. Therefore, the high-temperature flame generated by the combustion in the floor burners is close to the furnace wall and far from the reactor tubes, taking on a flat shape, which avoids the high-temperature flue gas burning the reactor tubes, because of direct contact with the reactor tubes. The high-temperature flue gas heats the furnace wall and reflects the radiant heat to the reactor tubes through the furnace wall. This feature not only prevents overheating in one part of the reactor tubes, but also improves the heating uniformity of the furnace. The latter also clearly indicates that treating the furnace surface with products such as Emisshield⁴⁷ could significantly increase the furnace efficiency.

Figure 11 gives a temperature contour at a plane through the crossover section at a height of 12 m. As can be seen from

Figure 11, the flue gas temperature is obviously high in the crossover section. This is because the flue gas velocity of the front wall side is bigger than that of the rear wall side. The high-temperature flue gas flowing from the radiation burners on the front wall has a short residence time in the radiation section; thus, some of the high-temperature flue gas does not have sufficient time to transfer heat to the reactor tubes and flows into the crossover section along the furnace wall, thus resulting in temperatures that are too high in the crossover section and a low heating efficiency of the radiation burners on the front wall side. One can also see, from this figure, that a local high-temperature zone appears in the rear wall side of the furnace and, in particular, around the outlet tube. The reason for this phenomenon is the accumulation of high-temperature flue gas in the top in the rear wall side, because of the recirculation zone.

Figure 12 shows the flue gas temperature profiles in different zones along the furnace height. The top two curves (solid and dash-dotted lines) represent the flue gas average temperature

profiles of the floor burner zone, on the front wall side and rear wall side, respectively. The middle curve (dotted line) is the flue gas average temperature profile of the entire furnace zone. The bottom two curves (dashed and double-dot-dashed lines) denote the flue gas average temperature profiles of the zone near the reactor tubes on the front wall side and the rear wall side. Comparing the top two curves, the flue gas temperature above the floor burners of the front wall side is higher than that of the rear wall side when the furnace height is <6 m. Near the radiation burners, the flue gas temperature above the floor burners of the front wall side is lower than that of rear wall side. The main reason is the asymmetric flue gas velocity distribution. Comparison of the bottom two curves indicates that the flue gas

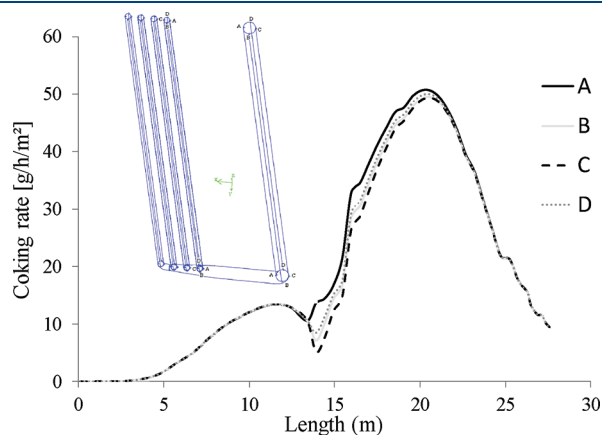


Figure 8. Simulated coking rate along the length of the reactor for four different circumferential positions A, B, C, and D in the coils.

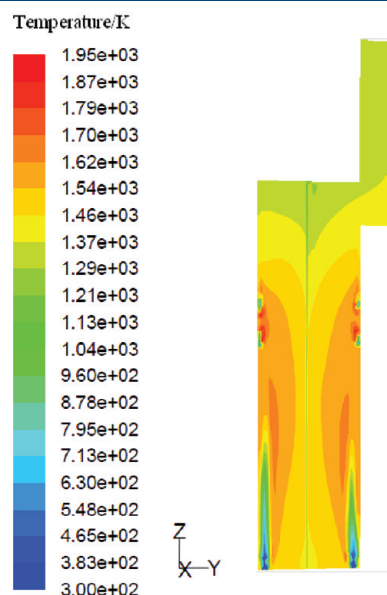


Figure 10. Flue gas temperature contour on the cross section at $x = 0.525$ m.

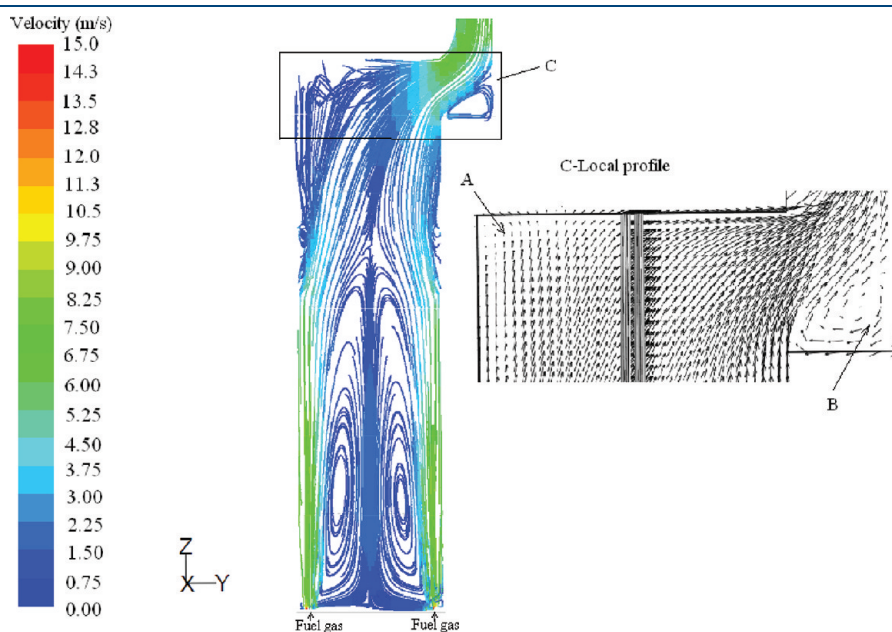


Figure 9. Flue gas velocity field at different heights in the plane located at $x = 0.525$ m.

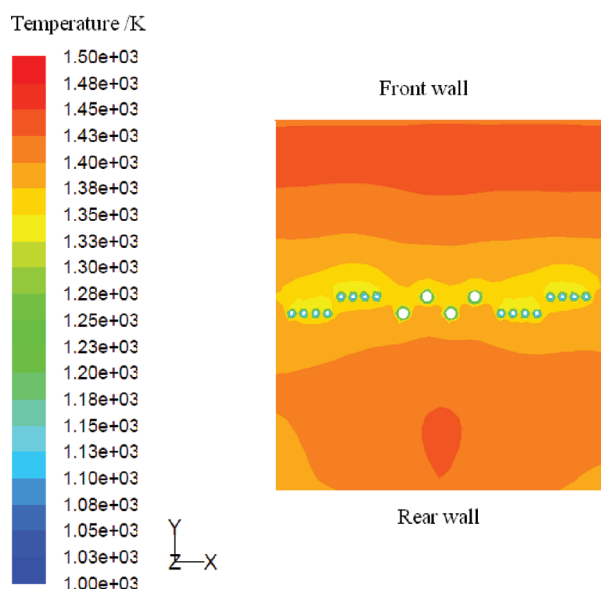


Figure 11. Temperature contour at a plane through the crossover section at a height of 12 m.

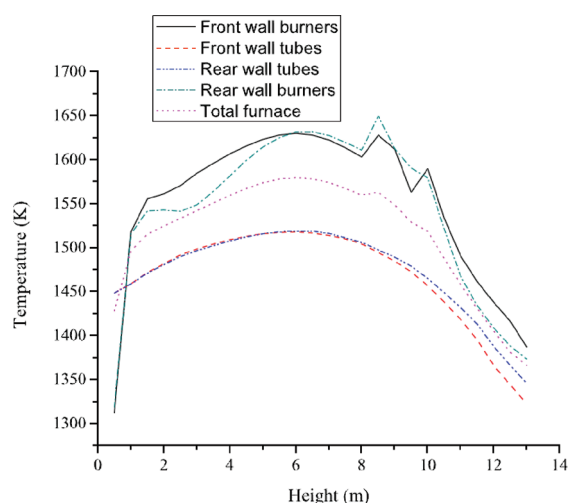


Figure 12. Flue gas temperature profiles in different zones along the furnace height.

temperature on the left tube (the rear wall side) is significantly higher than that on the right tube (the front wall side), especially above the radiation burners. This is because the high-temperature flue gas from radiation burners of the rear wall side should have been parallel to the wall for upward flow, but the high-temperature flue gas flows to the front wall side of furnace away from the original route, because of the asymmetry of flue gas velocity distribution and the obstruction effect of recirculation of the top of the furnace, thus leading to a large high-temperature surface at the rear wall side of the row of reactor tubes and a high-temperature flue gas flow that contacts with the tube walls on this side.

4.6. Flue Gas Concentration Profiles. In Figure 13, the mass fraction profile of flue gas above the floor burners along the furnace height is given. One can see that CO_2 and H_2O concentrations rapidly increase below 2.5 m in the furnace height

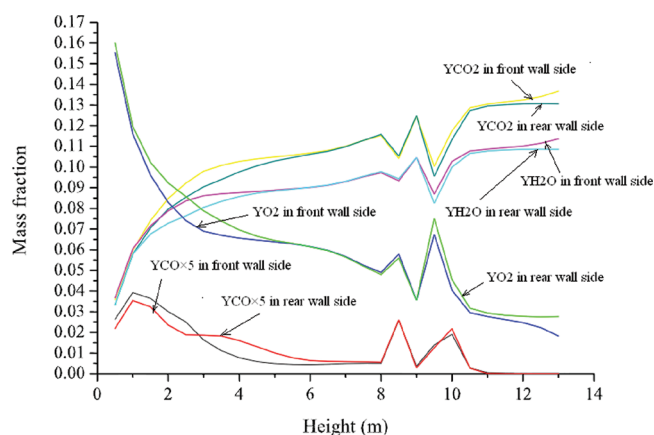


Figure 13. Mass fraction profiles of flue gas above the floor burners along the furnace height.

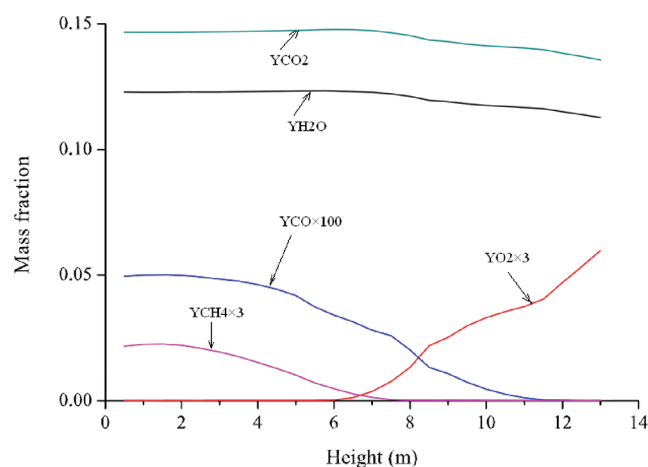


Figure 14. Mass fraction profiles of the flue gas in the zone near reactor tubes of the front wall side along the furnace height.

direction, while those of O_2 and CO gradually decrease, because of combustion. The profiles of CO_2 , H_2O , and O_2 concentrations in both the front wall side burners and rear wall side burners follow similar trends. In the radiation burner zone (i.e., a furnace height of 8–10 m), some fluctuations of the concentration of O_2 , H_2O , O_2 , and CO are observed. Near the radiation burners, the CO_2 and H_2O concentrations are low and the O_2 concentration is high, because of the combustion of fuel gas in the radiation burners. In the floor burner zone on the front wall side, the CO_2 and H_2O concentrations continuously increase along the furnace height, while the O_2 concentration decreases. In the floor burner zone of the rear wall side, the concentrations of CO_2 , H_2O , and O_2 are basically kept constant along the furnace height. The reason for this is that the outlet of the furnace is located on the front wall side, and all of the flue gases must pass through the central reactor tubes from the outlet into the convection section, which causes the asymmetrical flue gas flow in the top of the furnace. In the crossover section, the concentration of oxygen is low, because a large amount of O_2 with low concentration in the center of the furnace mixes with a small amount of O_2 with high concentration of the front wall side, while on the rear wall side, the O_2 with high concentration forms a “dead zone” at the corner of the top of furnace (see Figure 9).

Figure 14 typically shows the mass fraction profile of the flue gas in the zone near the reactor tubes of the front wall side along the furnace height. As can be seen from this figure, the CH_4 and CO concentrations decrease along the furnace height, because CH_4 is consumed via combustion. A large amount of CO is generated due to the incomplete combustion of CH_4 in the furnace bottom. With the increase in furnace height, the CO concentration gradually decreases, because of sufficient combustion of the fuel gas. At the bottom and middle of the furnace, the CO_2 and H_2O concentrations are high, while at the top, both have a slight reduction. The reason for both is that the flue gas recirculation brings most of CO_2 and H_2O to the bottom and middle of the furnace. In the top of the furnace, there is a relatively high O_2 concentration remaining, which is related to flue gas flow in the furnace. The remaining air flows in the high-speed jet zone where the flue gas is not recirculated to the furnace bottom (the point can be seen in Figure 9), but flows to the radiation outlet. The excessive O_2 leads to relatively high O_2 concentration in the top of the furnace, although some of the O_2 is consumed in the wall burners.

5. CONCLUSIONS

A coupled reactor/furnace simulation of an industrial SL-II naphtha cracking furnace with a capacity of 100 kt/yr is carried out for the first time, using a computational fluid dynamics (CFD) approach. Comparison with the measured industrial data of reactor and furnace shows that the simulation results agree well with industrial data and, hence, provide a theoretical guide for industrial practice. Without any modification to the kinetics, the simulated ethylene and propylene yields differ by <0.8 wt %, relative to the yields measured in the industrial naphtha cracking furnace. However, the differences observed for butadiene and benzene related to the use of a simplified molecular kinetic model for the kinetics show that it is necessary to introduce more-detailed chemistry in CFD models in the future, to further increase the agreement between industrial and measured data.

Our simulations further reveal that important radial gradients are observed in the reactor for the concentrations and the temperature that are not only caused by the heat flux from the fire side to the process gas side but also by the reactor design. The combination of floor and wall burners gives rise to a maximum of the coking rate near the middle of the second reactor pass and not at the reactor end, where the process gas reaches its maximum temperature.

Finally, the design of the radiation section outlet for this specific furnace makes the flue gas velocity near the front wall higher than that near the rear wall. Hence, the flue gas flowing from the radiation burners on the front wall has a shorter residence time than that at the rear wall, leading to a lower efficiency of the heat supply of the radiation burners, and causing locally some higher temperature in the crossover section.

■ ASSOCIATED CONTENT

Supporting Information. The results of the grid dependence study and the applied kinetics can be found in the Supporting Information. This material is available free of charge via the Internet at <http://pubs.acs.org>.

■ AUTHOR INFORMATION

Corresponding Author

*E-mail: fqian@ecust.edu.cn.

■ ACKNOWLEDGMENT

This work was supported by the National Science Fund for Distinguished Young Scholars (No. 60625302), 973 Program of China (No. 2012CB720500), National High-Tech Research and Development Program of China (No. 2009AA04Z159), and the Shanghai Leading Academic Discipline Project (No. B504). The financial support from the BOF Bilateral Scientific Cooperation (ECUST/LCT) and the Long Term Structural Methusalem Funding by the Flemish Government (No. BOF09/01M00409) and “111” Project by the Chinese Government (No. B08021) are acknowledged.

■ NOMENCLATURE

A, B = empirical constants

$C_{j,r}$ = molar concentration of species j in reaction r [kg mol/m^3]

C_{pi} = heat capacity of pure species i [J/(kg/K)]

$D_{i,m}$ = mass diffusion coefficient for species i in the mixture [m^2/s]

D_{ij} = binary mass diffusion coefficient of component i in component j [m^2/s]

D_t = effective mass diffusion coefficient due to turbulence [m^2/s]

E = total energy per unit mass [J/kg]

G_k = generation of turbulent kinetic energy [$\text{J/(m}^3/\text{s)}$]

h = sensible enthalpy [J/kg]

h_j = enthalpy of species j [J/kg]

I = radiation intensity [$\text{J/(m}^2/\text{s)}$]

J_j = diffusion flux of species j [$\text{kg/(m}^2/\text{s)}$]

k = turbulent kinetic energy [m^2/s^2]

k_{eff} = effective conductivity [W/(m/K)]

$k_{f,r}$ = forward rate constant for reaction r [$1/\text{s}$]

$k_{b,r}$ = backward rate constant for reaction r [$1/\text{s}$]

k_i = absorption coefficient of the i th gray gas [$1/\text{m}$]

k_t = turbulent thermal conductivity [W/(m/K)]

$M_{w,i}$ = molecular weight of species i [g/mol]

n = refractive index and refractive index

N = number of chemical species in the system

p = pressure and the sum of the partial pressures of all absorbing gases [Pa]

p_{eff} = effective pressure [Pa]

\vec{r} = position vector

R = ideal gas constant; $R = 8.314 \text{ J/(mol/K)}$

R_i = net rate of production of species i by chemical reaction [$\text{g mol/(m}^3/\text{s)}$]

R_j = rate of reaction in which j participates [kmol/(m/s)]

\vec{s} = direction vector

\vec{s}^T = scattering direction vector

s = path length

Sc_t = turbulent Schmidt number

S_h = source term in the energy equation [$\text{J/(m}^3/\text{s)}$]

T = local temperature and process-gas temperature [K]

U_i = velocity component in the i -direction [m/s]

U_j = velocity component in the j -direction [m/s]

U_l = velocity component in the l -direction [m/s]

x_i = coordinate direction in the i -direction [m]

x_j = coordinate direction in the j -direction [m]

x_l = coordinate direction in the l -direction [m]

X_i = mole fraction of species i

Y_j = mass fraction of species j

Y_P = mass fraction of product P

Y_R = mass fraction of reactant R

Greek Letters

α = absorption coefficient [1/m] and conversion factor depending on the units of p_t

$\alpha_{\varepsilon,i}$ = emissivity weighting factors for fictitious gray gas i

δ_{ij} = Kronecker delta

ε = dissipation rate of turbulent kinetic energy [m^2/s^3] and emissivity

ε/k = Lennard-Jones potential energy parameter [K]

μ = viscosity of gas molecules [$\text{kg}/(\text{m}/\text{s})$]

μ_{eff} = effective viscosity [$\text{kg}/(\text{m}/\text{s})$]

μ_t = turbulent viscosity [$\text{kg}/(\text{m}/\text{s})$]

ρ = gas density [kg/m^3]

Γ = net effect of third bodies on the reaction rate

$\nu'_{i,r}$ = stoichiometric coefficient for reactant i in reaction r

$\nu''_{i,r}$ = stoichiometric coefficient for product i in reaction r

$\eta'_{j,r}$ = rate exponent for reactant species j in reaction r

$\eta''_{j,r}$ = rate exponent for product species j in reaction r

σ = Stefan–Boltzmann constant; $\sigma = 5.672 \times 10^{-8} \text{ W}/(\text{m}^2 \text{ K}^4)$

σ_i = Lennard-Jones collision diameter of species i [\AA]

σ_s = scattering coefficient [1/m]

Φ = phase function

Ω' = solid angle

Ω_D = diffusion collision integral

$\Omega_{\mu i}$ = viscosity collision integration times of species i

REFERENCES

- Froment, G. F. Thermal Cracking for Olefins Production Fundamentals and Their Application to Industrial Problems. *Chem. Eng. Sci.* **1981**, 36 (8), 1271–1282.
- Vandamme, P. S.; Froment, G. F. Scaling up of Naphtha Cracking Coils. *Ind. Eng. Chem. Process. Des. Dev.* **1981**, 20, 366–376.
- Huang, S. N.; Qian, F.; Yu, J. S. Zone Method Used for Ethylene Cracking Furnace Modelling. *J. East China Inst. Chem. Technol.* **1992**, 18 (Supplement), 160–166.
- Xie, D. M.; Qian, F.; Yu, J. S. The Mathematical Model for Naphtha Pyrolysis in SRT-III Cracking Furnace. I. The Modelling and Calculation of Clean Tube. *Petrochem. Technol.* **1993**, 22 (12), 813–819.
- Xu, Q.; Chen, B. Z.; He, X. R.; Zhang, L. Simulation for Naphtha Pyrolysis in Clear Radiation Tube of SRT-IV Cracking Furnace. *Comput. Appl. Chem.* **2001**, 18 (3), 223–228.
- Detemmerman, T.; Froment, G. F. Three-Dimensional Coupled Simulation of Furnaces and Reactor Tubes for the Thermal Cracking of Hydrocarbons. *Rev. Inst. Fr. Pet.* **1998**, 53 (2), 181–194.
- Heynderickx, G. J.; Oprins, A. J. M.; Marin, G. B.; Dick, E. Three-dimensional flow patterns in cracking furnaces with long-flame burners. *AIChE J.* **2001**, 47 (2), 388–400.
- Oprins, A. J. M.; Heynderickx, G. J.; Marin, G. B. Three-dimensional asymmetric flow and temperature fields in cracking furnaces. *Ind. Eng. Chem. Res.* **2001**, 40 (23), 5087–5094.
- Oprins, A. J. M.; Heynderickx, G. J. Calculation of three-dimensional flow and pressure fields in cracking furnaces. *Chem. Eng. Sci.* **2003**, 58 (21), 4883–4893.
- Stefanidis, G. D.; Merci, B.; Heynderickx, G. J.; Marin, G. B. CFD simulations of steam cracking furnaces using detailed combustion mechanisms. *Comput. Chem. Eng.* **2006**, 30 (4), 635–649.
- Stefanidis, G. D.; Heynderickx, G. J.; Marin, G. B. Development of reduced combustion mechanisms for premixed flame modeling in steam cracking furnaces with emphasis on NO emission. *Energy Fuels* **2006**, 20 (1), 103–113.
- Stefanidis, G. D.; Merci, B.; Heynderickx, G. J.; Marin, G. B. Gray/nongray gas radiation modeling in steam cracker CFD calculations. *AIChE J.* **2007**, 53 (7), 1658–1669.
- Stefanidis, G. D.; Van Geem, K. M.; Heynderickx, G. J.; Marin, G. B. Evaluation of high-emissivity coatings in steam cracking furnaces using a non-grey gas radiation model. *Chem. Eng. J.* **2008**, 137 (2), 411–421.
- Han, Y. L.; Xiao, R.; Zhang, M. Y. Combustion and pyrolysis reactions in a naphtha cracking furnace. *Chem. Eng. Technol.* **2006**, 29 (1), 112–120.
- Lan, X. Y.; Gao, J. S.; Xu, C. M.; Zhang, H. M. Numerical simulation of transfer and reaction processes in ethylene furnaces. *Trans. Inst. Chem. Eng., Part A, Chem. Eng. Res. Des.* **2007**, 85 (A12), 1565–1579.
- Zhang, Z. H.; Huang, G. Q.; Wu, X. Numerical simulation of combustion of USC ethylene cracking furnace. *Chem. Ind. Eng. Prog.* **2008**, 27 (2), 255–260.
- Wang, G. Q.; Zhang, L. J. Numerical simulation of gas flow and heat transfer in cracking heater. *Petrochem. Technol.* **2005**, 34 (7), 652–655.
- Zhou, H. Z.; Jia, Z. G. Three dimensional numerical simulation of flow and combustion in firebox of ethylene cracking furnace. *Petrochem. Technol.* **2007**, 36 (6), 584–590.
- Hu, G. H.; Wang, H. G.; Qian, F. Numerical simulation on flow, combustion and heat transfer of ethylene cracking furnaces. *Chem. Eng. Sci.* **2011**, 66, 1600–1611.
- Kumar, P.; Kunzru, D. Modeling of naphtha pyrolysis. *Ind. Eng. Chem. Process. Des. Dev.* **1985**, 24, 774–782.
- Tao, W. Q. *Numerical Heat Transfer*, Second Edition; Xi'an Jiaotong University Press: Xi'an, PRC, 2001.
- Launder, B. E.; Spalding, D. B. The numerical computation of turbulent flows. *Comput. Methods Appl. Mech. Eng.* **1974**, 3, 269–289.
- Magnussen, B. F.; Hjertager, B. H. On mathematical models of turbulent combustion with special emphasis on soot formation and combustion. In *Proceedings from the 16th International Combustion Symposium*; The Combustion Institute: Pittsburgh, PA, 1976; pp 719–729.
- Huang, Z. Q.; Yang, G. J.; Yu, Z. H.; Zhang, Z. X. *Petrochemical Tube Furnace Simulation and Computer Calculations*; Chemical Industry Press: Beijing, 1993.
- Modest, M. F. *Radiative Heat Transfer*, Second Edition; Academic Press: New York, 2003.
- Van Geem, K. M.; Pyl, S. P.; Reyniers, M. F.; Vercammen, J.; Beens, J.; Marin, G. B. On-line analysis of complex hydrocarbon mixtures using comprehensive two-dimensional gas chromatography. *J. Chromatogr. A* **2010**, 1217 (43), 6623–6633.
- Pyl, S. P.; Hou, Z.; Van Geem, K. M.; Reyniers, M. F.; Marin, G. B.; Klein, M. T. Modeling the Composition of Crude Oil Fractions Using Constrained Homologous Series. *Ind. Eng. Chem. Res.* **2011**, 50 (18), 10850–10858.
- Pyl, S. P.; Van Geem, K. M.; Reyniers, M. F.; Marin, G. B. Molecular Reconstruction of Complex Hydrocarbon Mixtures: An Application of Principal Component Analysis. *AIChE J.* **2010**, 56 (12), 3174–3188.
- Van Goethem, M. W. M.; Kleinendorst, F. I.; Van Leeuwen, C.; Van Velzen, N. Equation-based SPYRO (R) model and solver for the simulation of the steam cracking process. *Comput. Chem. Eng.* **2001**, 25 (4–6), 905–911.
- Manca, D.; Buzzi-Ferraris, G.; Cuoci, A.; Frassoldati, A. The solution of very large non-linear algebraic systems. *Comput. Chem. Eng.* **2009**, 33 (10), 1727–1734.
- Plehiens, P. M.; Froment, G. F. Firebox Simulation of Olefin Units. *Chem. Eng. Commun.* **1989**, 80, 81–99.
- Van Geem, K. M.; Zajdlík, R.; Reyniers, M. F.; Marin, G. B. Dimensional analysis for scaling up and down steam cracking coils. *Chem. Eng. J.* **2006**, 15–19.
- Froment, G. F. Kinetics and Reactor Design in the Thermal Cracking for Olefins Production. *Chem. Eng. Sci.* **1992**, 47 (9–11), 2163–2177.
- Van Geem, K. M.; Heynderickx, G. J.; Marin, G. B. Effect of Radial Temperature Profiles on Yields in Steam Cracking. *AIChE J.* **2004**, 50 (1), 173–183.
- Wang, J. D.; Reyniers, M. F.; Van Geem, K. M.; Marin, G. B. Influence of silicon and silicon/sulfur-containing additives on coke formation during steam cracking of hydrocarbons. *Ind. Eng. Chem. Res.* **2008**, 47 (5), 1468–1482.

- (36) Hirschfelder, J. O.; Curtiss, C. F.; Bird, R. B. *Molecular Theory of Gases and Liquids*; John Wiley & Sons: New York, 1954.
- (37) Wang, F.; Xu, Y. Y.; Ren, J.; Li, Y. W. Experimental investigation and modeling of steam cracking of Fischer–Tropsch naphtha for light olefins. *Chem. Eng. Process.* **2010**, *49* (1), 51–58.
- (38) Colannino, J. Mathematical Models for Characterizing and Predicting Heat Flux Profiles from Ethylene Cracking Units. Presented at the *AIChE Annual Meeting Conference Proceedings*; American Institute of Chemical Engineers (AIChE): Houston, TX, 2007.
- (39) Niaei, A.; Towfighi, J.; Sadrameli, S. M.; Karimzadeh, R. The combined simulation of heat transfer and pyrolysis reactions in industrial cracking furnaces. *Appl. Thermal Eng.* **2004**, *24* (14–15), 2251–2265.
- (40) Heynderickx, G. J.; Cornelis, G. G.; Froment, G. F. Circumferential Tube Skin Temperature Profiles in Thermal-Cracking Coils. *AIChE J.* **1992**, *38* (12), 1905–1912.
- (41) Graff, M. J.; Albright, L. F. Coke deposition from acetylene, butadiene and benzene decompositions at 500–900 °C on solid surfaces. *Carbon* **1982**, *20* (4), 319–330.
- (42) Marek, J. C.; Albright, L. F. Coke Formation on Catalysts or in Pyrolysis Furnaces. Presented at the *182nd Meeting of the American Chemical Society*, New York, 1981.
- (43) De Schepper, S. C. K.; Heynderickx, G. J.; Marin, G. B. Modeling the Coke Formation in the Convection Section Tubes of a Steam Cracker. *Ind. Eng. Chem. Res.* **2010**, *49* (12), 5752–5764.
- (44) Van Geem, K. M.; Dhuyvetter, I.; Prokopiev, S.; Reyniers, M. F.; Viennet, D.; Marin, G. B. Coke Formation in the Transfer Line Exchanger during Steam Cracking of Hydrocarbons. *Ind. Eng. Chem. Res.* **2009**, *48* (23), 10343–10358.
- (45) Zimmermann, H.; Walzl, R. Ethylene. In *Ullmann's Encyclopedia of Industrial Chemistry*; John Wiley & Sons: New York, 2009.
- (46) Gyorffy, M.; Hineno, M.; Hashimoto, K.; Park, S. H.; You, M. S. MERT Performance and Technology Update. Presented at the *AIChE Spring Meeting*, Tampa, FL, 2009.
- (47) Olver, J. Emisshield: Application to Pyrolysis Furnaces. Presented at the *AIChE Spring Meeting*, New Orleans, LA, 2008.